Biophysical Journal
Article

Biophysical Society

A vesicle microrheometer for high-throughput viscosity measurements of lipid and polymer membranes

Hammad A. Faizi,[1] Rumiana Dimova,[2] and Petia M. Vlahovska[3,*]
[1]Department of Mechanical Engineering, Northwestern University, Evanston, Illinois; [2]Department of Theory and Bio-Systems, Max Planck Institute of Colloids and Interfaces, Science Park Golm, Potsdam, Germany; and [3]Department of Engineering Sciences and Applied Mathematics, Northwestern University, Evanston, Illinois

ABSTRACT Viscosity is a key property of cell membranes that controls mobility of embedded proteins and membrane remodeling. Measuring it is challenging because existing approaches involve complex experimental designs and/or models, and the applicability of some methods is limited to specific systems and membrane compositions. As a result there is scarcity of systematic data, and the reported values for membrane viscosity vary by orders of magnitude for the same system. Here, we show how viscosity of membranes can be easily obtained from the transient deformation of giant unilamellar vesicles. The approach enables a noninvasive, probe-independent, and high-throughput measurement of the viscosity of membranes made of lipids or polymers with a wide range of compositions and phase state. Using this novel method, we have collected a significant amount of data that provides insights into the relation between membrane viscosity, composition, and structure.

SIGNIFICANCE Cell membranes are thin sheets whose fluidity is essential for processes that involve deformations or diffusion of membrane-associated biomolecules. Despite its importance, membrane fluidity remains poorly characterized because existing methods to determine membrane viscosity rely on complex experimental designs and analyses. Here, we devise a noninvasive, high-throughput method capable of measuring the viscosity of membranes with a wide range of compositions and phase state. The amassed data provide insights into the relation between membrane viscosity, composition, and structure. The method paves the way to quantify membrane fluidity in a fast and consistent manner, which will advance the understanding of cell membrane dynamics.

INTRODUCTION

Cells and cellular organelles are enveloped by membranes, whose main structural component is a lipid bilayer (1). The lipid bilayer endows membranes with fluidity that is essential for functions that depend on biomolecule mobility, e.g., signaling (2–4). Fluidity is modulated by membrane composition, and this homeoviscous adaptation is crucial for the survival of organisms that cannot regulate their body temperature, such as bacteria (5,6). Viscosity is the common measure for fluidity, yet for membranes this property has been challenging to assess. Data for viscosity of lipid membranes are limited and reported values vary significantly, sometimes by orders of magnitude for the same system (Appendix Table 1).

For example, reported values for the surface shear viscosity of membranes made of a typical lipid such as dioleoylphosphatidylcholine (DOPC) span two orders of magnitude: $(0.197 \pm 0.0069) \times 10^{-9}$ Pa·s·m (7), $(1.9 \pm 11) \times 10^{-9}$ Pa·s·m (8), $(16.72 \pm 1.09) \times 10^{-9}$ Pa·s·m (9). For a similarly structured lipid, palmitoyloleoylphosphatidylcholine (POPC), the surface viscosity measured by shear rheology of Langmuir monolayers is 3×10^{-4} Pa·s·m (10). Experimental methods that utilize free-standing bilayer membranes, e.g., vesicles or black lipid membranes, rely on estimates from the rate of tether formation (11), diffusion coefficients of domains (12–14) or membrane-anchored particles (15,16,17), domain shape fluctuations (18), domain motion on vesicles induced by applied flow (8,19), bilayer thickness fluctuations or lipid dynamics measured with neutron spin echo spectroscopy (20–22), fluorescence quantum yield or lifetime of

Submitted October 21, 2021, and accepted for publication February 9, 2022.

*Correspondence: petia.vlahovska@northwestern.edu

Editor: Andreas Janshoff.

https://doi.org/10.1016/j.bpj.2022.02.015

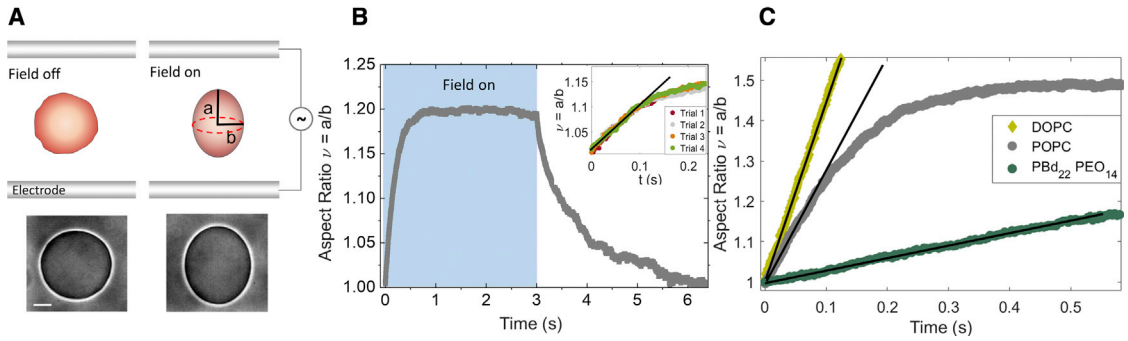

FIGURE 1 Vesicle electrodeformation reveals differences in membrane viscosity. (*A*) A uniform electric field deforms a GUV into a prolate ellipsoid by pulling out area stored in suboptical thermally excited membrane undulations. Snapshots of the vesicle during the experiment. Imaging with phase contrast microscopy. Scale bar, 15 μm. (*B*) Prolate deformation of a POPC GUV in an electric field with amplitude $E_0 = 10$ kV/m and frequency of 1 kHz. Time zero in all graphs corresponds to turning the field on. The inset shows that repeated deformation does not alter the initial slope of the deformation curve. Because of the applied field forcing, deformation while the electric field is on is much faster than the relaxation driven by the membrane tension; the characteristic timescale of electrodeformation, $\eta/\varepsilon E_0^2$, is much shorter than the relaxation timescale, $\eta R/\sigma$. (*C*) Vesicles made of lipids (DOPC, POPC) and the diblock copolymer $PBD_{22}PEO_{14}$ deform at a different rate indicating different membrane viscosity. The field strength and frequency are 8 kV/m and 1 kHz. The solid lines correspond to the theoretical fit with Eq. 2. To see this figure in color, go online.

viscosity-sensitive fluorescent dyes (23,24), and the forced motion of colloidal particles in the membrane (25–27). In silico approaches, using molecular dynamics simulations, have also been developed to determine membrane viscosity (7,28,29). Despite these advances, the systematic study of membrane viscosity has been hindered by various limitations of the proposed methodologies. For example, domain-based methods (8,12,13,18,19) are limited to phase-separated membranes, and the measured viscosity reflects the continuous phase, not the membrane as a two-phase fluid. Bilayer thickness fluctuations (20) depend on both shear and dilational monolayer viscosities. In particle-based methods (15,16,25–27), the probe perturbs the membrane and the data interpretation requires complicated analysis that discerns the contributions to the particle mobility from the flow in the membrane and the surrounding fluids (30–32). Furthermore, since membrane surface viscosity is a macroscopic quantity defined on scales where the bilayer can be modeled as a two-dimensional incompressible fluid, methods utilizing measurements at the micro- or nano-scale and/or based on molecular probes may not report the effective continuum viscosity but a quantity, often called "microviscosity," which is local and depends on the immediate environment (22). These complexities are likely the source of the huge variability in reported values of viscosity for lipid bilayer membranes, making it challenging to compare data obtained by different methods.

Here, we show that the time-dependent deformation of giant unilamellar vesicles (GUVs) can be employed to obtain the surface "macroviscosity," i.e., the shear viscosity of the membrane treated as a two-dimensional incompressible fluid. Upon application of an extensional stress, e.g., generated by an uniform electric field (33–36), extensional flow (37–39), or an optical stretcher (40,41) a quasi-spherical vesicle deforms into a prolate ellipsoid. The aspect ratio, $\nu = a/b$ (see sketch in Fig. 1 *A*), increases and reaches a steady state. When the stress is removed, the vesicle relaxes back to its equilibrium spherical shape. Fig. 1 *B* and Video S1 illustrate this process for a vesicle in a uniform electric field. Vesicle electrodeformation has been used to measure bending rigidity of membranes from the steady-state shapes (maximum deformation at a given electric field strength) (42–45). Here, we show that the time-dependent shapes can yield membrane viscosity. Even though the applied stress is extensional and vesicle deformation is axisymmetric, material transported on the vesicle surface undergoes shear because the membrane is area-incompressible (46–50). The rate at which the vesicle elongates while the field is on, and relaxes back to its equilibrium shape after the field is turned off, is related to the membrane shear viscosity. For small deformations, $\nu \lesssim 1.5$, the evolution of the aspect ratio is described by (35,50–52) (see Supporting material, section 1 for a summary of the theory)

$$\dot{\nu} = \frac{1}{\eta(55 + 16\chi_m)}\left(3p - \frac{24\sigma}{R}(\nu - 1)\right), \qquad (1)$$

where $\chi_m = \eta_m/\eta R$ is the dimensionless surface viscosity η_m, η is the viscosity of the solution inside and outside the vesicle (assumed to be the same), σ is the membrane tension, and R is the vesicle radius. In an applied extensional flow with strain rate $\dot{\gamma}$, $p = 60\eta\dot{\gamma}$. In the case of a charge-neutral vesicle in a uniform DC electric field with amplitude E_0, $p = 9\varepsilon E_0^2/4$, where ε is the permittivity of the solution, and in an AC field with frequency ω, $p(\omega)$ is given in Supporting material, section 1 (note that the permittivity is constant in the frequency range used for the experiments). Thus, from the vesicle dynamics in response to an extensional flow or a uniform electric field it is straightforward to obtain the membrane viscosity. Note that the dynamics does not involve dilational viscosity because vesicle deformation and the accompanying increase in apparent area come from ironing of suboptical thermally excited membrane undulations, while the area per lipid remains the same.

MATERIALS AND METHODS

Vesicle preparation

GUVs are formed from lipids and polymers such as POPC, DOPC, oleoylmyristoylphosphatidylcholine (OMPC), cholesterol (Chol), stearoyloleoylphosphatidylcholine (SOPC), dipalmitoylphosphatidylcholine (DPPC), and poly(butadiene)-*b*-poly(ethylene oxide) diblock copolymers, PBd_x-*b*-PEO_y. The lipids and diblock copolymers were purchased from Avanti Polar Lipids (Alabaster, AL) and Polymer Source (Montreal, Canada), respectively. The multicomponent vesicles made of DOPC:DPPC:Chol were fluorescently marked with 0.1 mol % of Liss Rhod PE. The lipid vesicles were produced using the electroformation method (53). The stock solutions of 12 mM lipid in chloroform are diluted to 5 mM from which 10 μL of the solution is spread on the conductive sides of the ITO slides (Delta Technologies, Loveland, CO). The slides are stored in a vacuum for 2–4 h to evaporate all the organic solvents. The two slides are then sandwiched with a 2-mm-thick Teflon spacer, and the electroformation chamber is filled with 40 mM sucrose solution in 0.3 mM of NaCl. The conductivity conditions were chosen to ensure prolate deformation (34). The chamber is connected to a signal generator (Agilent, Santa Clara, CA) for 2 h at 50 Hz and voltage 1.5 V at 60°*C*, which ensures that all lipids are above their main phase transition temperatures. The harvested vesicles are diluted in isotonic glucose solution without salt. Three independent GUV batches for every lipid composition were analyzed. Polymer vesicles were produced from a spontaneous swelling method. Initially, 50 μL of 6–10 mg/mL (in chloroform) polymer solution was dissolved in 200–300 μL of chloroform in a 20 mL vial. Polymer films were formed from evaporation by blowing with a nitrogen stream while swirling the solution inside. Thereafter, the vials were dried under vacuum for 2–4 h. The polymer films were hydrated in the suspending solutions (40 mM sucrose solution in 0.3 mM NaCl) and placed at 60°C in an oven for 18–24 h.

Electrodeformation

The electrodeformation experiments are conducted in the electrofusion chamber (Eppendorf, Hamburg, Germany). The chamber is made from Teflon with two 92 μm cylindrical parallel electrodes 500 μm apart. The field is applied using a function generator (Agilent 3320A). The function generator is controlled using a custom-built MATLAB (MathWorks, Natick, MA) program. This gives precise control over the strength and duration of applied electric fields (45). Electric fields with amplitude up to 10 kV/m and frequency up to 1 kHz were used.

Optical microscopy and imaging

The vesicles are visualized using a phase contrast microscope (A1 Axio Observer; Zeiss, Jena, Germany) with 63× objective 0.75 NA (air). Imaging is performed using a Photron (San Diego, CA) SA1.1 camera. The image acquisition rate for electrodeformation recordings is kept to a constant of 500–2000 frames per second (fps) for lipid vesicles and 60–200 fps for polymer vesicles, and the shutter speed is fixed to 500 μs. The time evolution of the vesicle is analyzed using home-made image analysis software. The software uses a Fourier series to fit around the vesicle contour, $r_s = \sum_{n=0}^{\infty}\alpha_n\cos(n\theta) + \beta_n\sin(n\theta)$. The second mode in the series is used to determine the major axis (a) and minor axis (b) of the deformed vesicles to evaluate $\nu = \frac{a}{b} = (1+\alpha_2)/(1-\alpha_2)$.

Bending rigidity and tension measurements

Flickering spectroscopy is a popular technique to extract membrane rigidity and tension, due to its nonintrusive nature and well-developed statistical analysis criteria. The details of the technique are given in (44,54,55). Essentially, a time series of fluctuating vesicle contours is recorded on the focal plane. The quasi-circular contour is represented in Fourier modes, $r(\varphi) = R(1+\sum_q u_q(t)\exp(iq\varphi))$. The fluctuating amplitudes u_q have mean square amplitude dependence on the membrane bending rigidity κ and the tension σ, $\langle|u_q|^2\rangle \sim \frac{k_BT}{\kappa(q^3+\bar{\sigma}q)}$, where k_BT is the thermal energy (k_B is the Boltzmann constant and T is the temperature), and $\bar{\sigma} = \sigma R^2/\kappa$. The integration time effect of the camera was reduced by acquiring images at a low shutter speed of 100–200 μs. At least 5000 images were obtained for each vesicle for good statistics.

RESULTS

We illustrate the implementation of the approach with the example of a quasi-spherical vesicle subjected to a uniform AC electric field. The electric field is advantageous over extensional flow or radiation pressure (as in optical stretchers) because of the simplicity of the experimental setup and the ability to analyze multiple vesicles at the same time, which highly speed up the measurements. The use of an AC field is preferable because a DC field could cause Joule heating and electro-osmotic flows, whose effect on vesicle deformation and stability is difficult to account for (56). We applied the method to fluid membranes composed of the phosphatidylcholine lipids palmitoyloleoyl (POPC), dioleoyl (DOPC), oleoylmyristoyl (OMPC), stearoyloleoyl (SOPC), and dipalmitoyl (DPPC), Chol, and diblock copolymers PBd_x-*b*-PEO_y with varying hydrophobic molecular weight, M_h, from 0.7 kDa to 6.8 kDa.

Vesicle transient deformation yields membrane viscosity

Fig. 1 summarizes the experiment. The elongation curves of a GUV initially show linear increase (Figs. 1 *C* and S4). The linear slope is predicted by Eq. 1 if the second term, which describes the action of the tension opposing the deformation, is neglected:

$$\nu = 1 + \frac{t}{t_d}\left(\frac{3p(\omega)}{(55+16\chi_m)}\right), \tag{2}$$

where $1/t_d = \varepsilon E_0^2/\eta$ is the characteristic rate of strain imposed by the electric field. Thus, the slope of the aspect ratio plotted as a function of the rescaled time t/t_d, at the same field frequency, depends solely on the membrane viscosity. Vesicles made of different lipids or diblock copolymers show different initial slopes (see Fig. 1 *C*), indicating different membrane viscosities. The linear response is observable only if the restoring force of the membrane tension is negligible compared with the deforming electric stress, i.e., $\sigma/R\varepsilon E_0^2 \ll 1$, which is indeed the case for typical values of the applied electric field $E_0 = 8$ kV/m, equilibrium membrane tension $\sigma = 10^{-8}$ N/m, and vesicle radius $R = 10$ μm. The time up to which the linear approximation is reasonable (see Supporting material, section 1B) is estimated to be $t_c/t_d \sim \varepsilon E_0^2 R(55+16\chi_m)/(12\sigma)$. Using times up to $0.1t_c/t_d$ (or equivalently ν up to 1.1) minimizes the error in the linear fit. Even though the whole deformation curve could

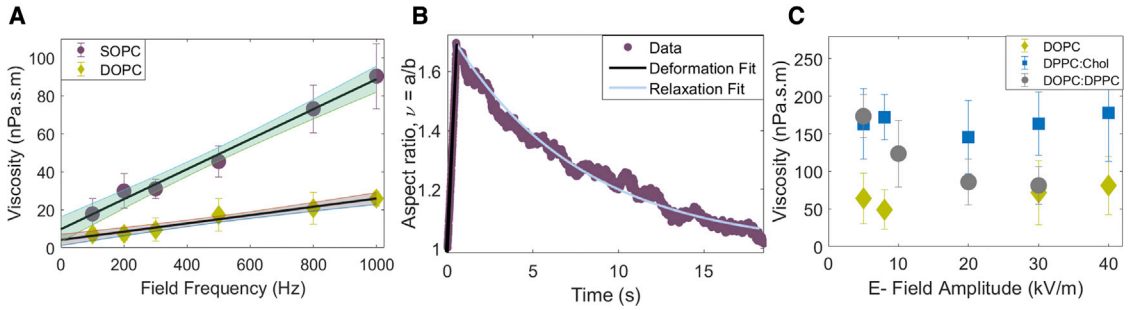

FIGURE 2 (*A*) Viscosity measured at different frequencies at a fixed field strength 8 kV/m increases with frequency. Extrapolating to zero frequency yields the shear surface viscosity. The symbols on the vertical-axis intercept refer to the extrapolated values of 4.11 ± 2.63 nPa·s·m and 9.73 ± 5.80 nPa·s·m for DOPC and SOPC, respectively. The R-squared value of the linear fit is 0.98 and 0.97 for the SOPC and DOPC, respectively. The shaded band represents a 95% confidence interval. (*B*) Shape relaxation after the field is turned off yields a similar value for the viscosity as the zero-frequency limit obtained from the frequency sweep. Data for SOPC, $E_0 = 8$ kV/m and $\omega = 1$ kHz. Tension obtained from flickering spectroscopy is 5.7 ± 2.6 × 10^{-9} N/m. Viscosity obtained from initial deformation and relaxation is 164 nPa·s·m and 21.1 ± 29.4 nPa·s·m, respectively. (*C*) Viscosity of single-component (DOPC) and single-phase multicomponent (DPPC:Chol 1:1) bilayers is independent of field magnitude, in contrast to the viscosity of phase-separated multicomponent (DPPC:DOPC 1:1) bilayers. To see this figure in color, go online.

be fitted using Eq. 1, the nonlinear fit with two parameters (viscosity and tension) or three parameters, if bending rigidity is also unknown, is challenging. Since Eq. 2 implies single-parameter fitting, we consider its use to yield more reliable viscosity results (especially for more viscous membranes). Furthermore, it eases the implementation of data fitting. The reproducibility of the results was tested by repeated measurements with the same vesicle (see Fig. 1 *B*, inset), showing identical slope of the aspect ratio curves for small deformations. Fig. S3 demonstrates that analyzing vesicles made in different preparations and on different days also results in consistent values.

Effects of field frequency and amplitude

Intriguingly, measurements at the same field amplitude but different frequencies revealed an apparent increase of viscosity with frequency (Fig. 2 *A*). Viscosity values in the literature obtained by methods that do not involve electric fields (Appendix Table 1) are at least a factor of 10 smaller than the value of the viscosity measured at 1 kHz but comparable with the zero-frequency limit obtained from the linear extrapolation at low frequencies. We hypothesize that the zero-frequency viscosity is representative of the viscosity of the membrane in the absence of electric field. As a test, we analyzed the vesicle relaxation back to its equilibrium shape after the field is turned off (Fig. 2 *B*). That analysis, however, is complicated by the fact that unlike the initial elongation upon application of the field, the relaxation is driven by and thus depends on the membrane tension. To leave the membrane viscosity as the only fitting parameter for the relaxation curve, the tension needs to be independently determined. In this experiment, the tension was obtained from the analysis of the equilibrium thermally excited membrane undulations (flickering spectroscopy) in the absence of an electric field before the electrodeformation experiment. The fit of the relaxation curve with Eq. 1 yielded viscosity 21.1 ± 29.4 nPa·s·m. The large error is due to the uncertainty in the tension. The viscosity value is close to the zero-frequency limit of the viscosity obtained from the frequency sweep (9.73 ± 5.80 nPa·s·m) for SOPC. We adopt the frequency sweep to determine the initial linear dependence of the viscosity and its "no-field" limit.

Electric field decreases the melting temperature of DPPC:DOPC:Chol bilayers (57), thus suggesting field-dependent membrane fluidity. We find that bilayers made of only one lipid or a homogeneous mixture, either in the liquid-disordered (e.g., DOPC or POPC) or liquid-ordered (e.g., DPPC:Chol 1:1) state, exhibit field-independent viscosity. However, the phase-separated bilayers such as DPPC:DOPC (1:1), which have solid domains coexisting with liquid-disordered continuous phase (58–60), showed viscosity decrease with increasing field amplitude (Fig. 2 *C*).

Method summary

To summarize, the method involves measuring apparent viscosities at different frequencies in the range 0.1–1 kHz and extrapolating to zero frequency (as in Fig. 2 *A*) to obtain the value of the viscosity in the absence of an electric field. An electric field of 8 kV/m produces a good range of data in the initial linear deformation regime. The method is high-throughput as it allows measurement of several vesicles at the same time; measurement and data analysis of each vesicle typically take about 10 min. We analyze 10–50 vesicles per viscosity value. The viscosity obtained for 14 different bilayer compositions is reported in Table 1. The values are in the range reported in previous studies (Appendix Table 1). For example, the bilayer viscosity for SOPC is in good agreement with previously reported values from 3 to 13 nPa·s·m (27,28,61).

TABLE 1 Membrane viscosity and bending rigidity for various bilayer systems at 25.0°C and $E_0 = 8$ kV/m

Composition	Viscosity (nPa·s·m)	Bending rigidity (k_BT)
DOPC	4.11 ± 2.63	22.2 ± 2.0
OMPC	7.73 ± 3.09	27.1 ± 2.6
POPC	9.32 ± 5.95	27.8 ± 2.3
SOPC	9.73 ± 5.80	30.1 ± 3.1
DOPC:Chol	7.00 ± 4.77	27.8 ± 4.6
DPPC:DOPC:Chol (1:1:1)	17.7 ± 3.06	72.0 ± 8.4
DPPC:DOPC:Chol (1:1:2)	15.4 ± 2.40	69.2 ± 7.9
DPPC:Chol (1:1)	56.4 ± 4.63	121.3 ± 11.0
PBd_{13}-*b*-PEO_{11}	14.4 ± 4.40	17.1 ± 1.5
PBd_{22}-*b*-PEO_{14}	686 ± 51.0	31.0 ± 5.1
PBd_{33}-*b*-PEO_{20}	2890 ± 670	54.4 ± 6.4
PBd_{46}-*b*-PEO_{24}	20,600 ± 4700	NA
PBd_{54}-*b*-PEO_{29}	46,700 ± 900	154.0 ± 16.0
PBd_{120}-*b*-PEO_{78}	157,000 ± 54,500	NA

Viscosity correlation with lipid diffusivity, membrane composition, and thickness

Since mobility of lipids or domains is often used to assess membrane fluidity (12–14), we have compared our results for membrane viscosity with measurements of the diffusion coefficient of a lipid dye (DiI-C18) using fluorescence correlation spectroscopy (FCS) in the same ternary system (62). The diffusion coefficient scales inversely with surface viscosity (Fig. 3), a trend expected from the Saffman-Delbrück model (63), $D = k_BT(\log(\eta_m/(\eta r)) - 0.5772)/(4\pi\eta_m)$. However, there is a quantitative disagreement: using lipid dye radius $r = 0.5$ nm (comparable with the radius of DOPC estimated from the area per lipid head, 67.4–75.4 Å^2 (64–69)), the Saffman-Delbrück equation predicts much lower diffusivities. These results suggest that while increasing viscosity does correlate with decreasing diffusivity, it is not trivial to relate membrane viscosity and the diffusion constant because diffusion of molecular probes is sensitive to the probe itself as well as the bilayer structure (11,14,22).

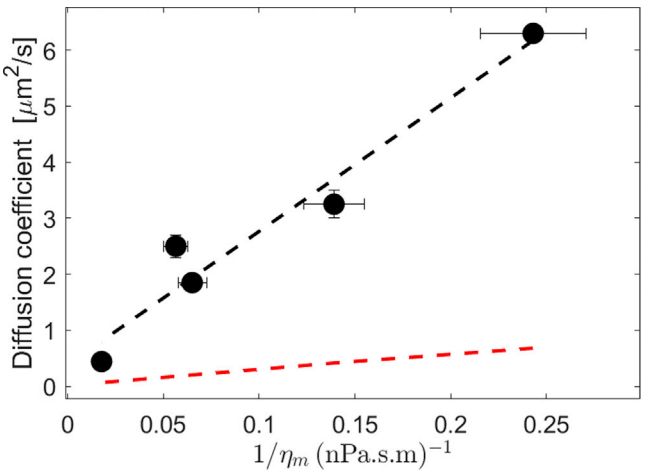

FIGURE 3 Membrane viscosity as a function of diffusivity values obtained with FCS (62) for membrane compositions DOPC, DOPC:Chol (1:1), DPPC:DOPC:Chol (1:1:2), DPPC:DOPC:Chol (1:1:1), and DPPC:Chol (1:1). Values of the diffusion coefficient are listed in Table S2. The red dashed line corresponds to the prediction from the Saffman-Delbrück model with probe radius $r = 0.5$ nm. The black dashed line is a linear fit with intercept 0.383 μm^2/s and slope 23.83 μm^3·mPa. To see this figure in color, go online.

The viscosity values compiled in Table 1 highlight that in pure lipid systems membrane viscosity decreases with the number of unsaturated bonds in the hydrophobic tail. POPC, OMPC, and SOPC have a single unsaturated bond while DOPC has two double bonds in the hydrophobic tails. DOPC bilayers exhibit much smaller viscosity than the other single unsaturated lipid bilayers. In the mixed systems, adding DPPC or/and Chol to DOPC increases the viscosity. Adding Chol (molar ratio 1:1) to DOPC increases the bilayer viscosity as Chol increases the packing of the liquid-disordered (L_d) phase. For the liquid-ordered (L_o) phase, such as DPPC:Chol (1:1), the bilayer viscosity is much higher due to the tight packing provided by saturated acyl chains. The effect is less pronounced in the ternary L_o system DOPC:DPPC:Chol (1:1:2) and DOPC:DPPC:Chol (1:1:2). For a phase-separated system of coexisting solid and fluid phases DOPC:DPPC (1:1) (see Fig. 2 *B*), the viscosity also increases relative to pure DOPC. The increase agrees with an estimate of the viscosity of a two-dimensional (2D) suspension, $\eta_{\text{eff}} = \eta_{\text{DOPC}}(1 + 2\varphi)$, where $\varphi \sim 0.4$ is the fraction of the solid phase (70).

Using our method we examined the commonly assumed relation between the 2D viscosity (η_m) and three-dimensional (3D) viscosity (η_{3D}), $\eta_m = \eta_{3D}h$, where h is the membrane thickness. The thickness of diblock-polymer bilayers increases with the molecular weight of the hydrophobic part, $h \sim M_h^n$ (71,72), where n lies within the theoretical bounds of 0.5 (random Gaussian coil) and 1 (full stretch). The polymers' molecular weight varies in a wide range (1–8 kDa), thereby resulting in bilayers with greater range of thicknesses, unlike lipids. The diblock polymers showed membrane viscosity spanning four orders of magnitude, from 14 nPa·s·m to 157,000 nPa·s·m. The lowest-molecular-weight polymer membrane exhibits a viscosity similar to that of POPC. Fig. 4 *A* shows that the membrane viscosity does follow a power-law dependence on M_h, but the power 5.6 is much larger than the expected range of 0.5–1. In contrast, as seen from Fig. 4 *B*, the bending rigidity follows a power law consistent with the expected $\kappa \sim M_h^{2n}$, since $\kappa/K_A \sim h^2$, where K_A is the area-compressibility modulus (73). The K_A value is relatively insensitive to the molecular weight; its value for the lipids was taken to be 250 mN/m and for the polymer membranes 100 mN/m (74,75). The polymer 3D viscosity η, however, varies with the polymer molecular weight, and this may be the source of the unexpectedly higher exponent in the power-law dependence of η_m on M_h.

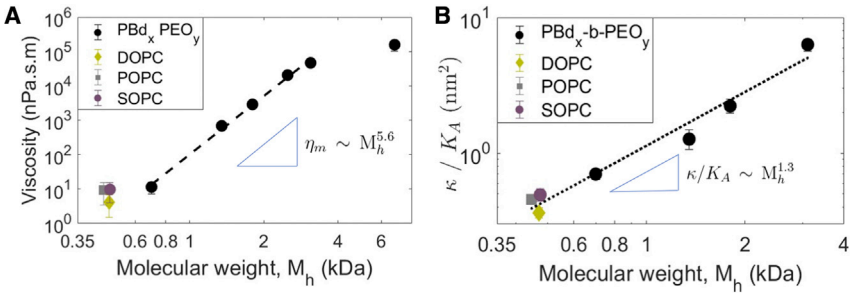

FIGURE 4 (*A*) Viscosity of PBd$_x$-*b*-PEO$_y$ bilayers as a function of the M_h of the hydrophobic part (PBd). Viscosities of phospholipids are also shown for comparison. (*B*) Bending rigidity κ (scaled by the area-compressibility modulus K_A) of PBd$_x$-*b*-PEO$_y$ and phospholipid bilayer membranes as a function of molecular weight. The power law obtained is $\kappa/K_A \sim M_h^{1.3}$. The values of the bending rigidity are listed in Table S1. To see this figure in color, go online.

CONCLUSIONS

We developed a novel method to measure the shear viscosity of membranes using the transient deformation of a giant vesicle. The approach is inspired by the interfacial rheology measurements using deformation of droplets and capsules (76). The method is able to interrogate a wide range of bilayer compositions and phase states, and the measured membrane viscosities span a range of more than four orders of magnitude. The collected data show that decreasing viscosity leads to increasing probe diffusivity, although the relation is not captured by the celebrated Saffman-Delbrück equation. Membrane viscosity is also found to nontrivially depend on bilayer thickness. Using diblock-copolymer systems with different molecular weight to modulate bilayer thickness revealed a power-law relation between viscosity and molecular weight that is much stronger than the power predicted from the assumption that the membrane viscosity is equal to the bulk viscosity multiplied by bilayer thickness. Our study also reveals that viscosity is sensitive to membrane electric polarization. In an applied uniform electric field, membrane viscosity increases with frequency, while in some systems electric field amplitude has the opposite effect. For example, the macroviscosity of phase-separated gel-fluid membranes decreases with the field magnitude. These findings open new questions for future exploration.

The ease of implementation, high throughput, minimal experimental equipment and effort, as well as robustness make the electrodeformation viscometry developed by us easy to adopt in every lab. The method can also be applied to obtain interfacial properties of lipid monolayers using deformation of droplets and fitting the shape evolution with the theoretical model in (52). Such study will hopefully shed some light on the observed discrepancies between monolayer and bilayer viscosities (77,78). We envision that our approach will become a standard tool for characterization of membrane fluidity that will help address questions of biological and engineering importance such as synthetic cell design.

SUPPORTING MATERIAL

Supporting material can be found online at https://doi.org/10.1016/j.bpj.2022.02.015.

APPENDIX

See Appendix Table 1.

APPENDIX TABLE 1 Membrane viscosity obtained using different experimental methods and simulations

Method	Membrane composition	Viscosity (nPa·s·m)	Temperature (K)	System
Falling ball viscometry (27)	SOPC	3	298	GUVs
Coarse-grained simulations (28)	SOPC	3	323	bilayer
Electrodeformation (this study)	SOPC	9.73 ± 5.80	298	GUVs
Probe diffusion (61)	SOPC	13.2 [a]	293	GUVs
Optical dynamometry (26)	DMPC	5 ± 2	298	GUVs
Neutron spin echo (20)	DMPC	75	298	SUVs
Coarse-grained simulations (28)	DMPC	5	323	bilayer
Fluorescence spectroscopy (79)	DMPC	0.36 [a]	298	SUVs
Tether pulling (11)	EPC	2.7–88	295–298	GUVs
Shear surface rheology (10)	POPC	300,000	NA	monolayer
Electrodeformation (this study)	POPC	9.32 ± 5.95	298	GUVs
Shear surface rheology (10)	POPC:Chol (7:3)	10,000	NA	monolayer
Shear surface rheology (10)	DPPC	900,000	NA	monolayer
Optical tweezers (80)	DOPC	<0.6	293	bilayer
Fluorescence spectroscopy (79)	DOPC	0.20 [a]	298	SUVs
Fluorescence quantum yield (23)	DOPC	0.84 [a]	298	LUVs
Fluorescence lifetime of dye (24)	DOPC	0.15 [a]	298	LUVs

(*Continued on next page*)

Appendix Table 1. *Continued*

Method	Membrane composition	Viscosity (nPa·s·m)	Temperature (K)	System
All-atom simulations (7)	DOPC	0.197 ± 0.0069	297	bilayer
Coarse-grained simulations (28)	DOPC	0.17	323	bilayer
Membrane-anchored particles (16)	DOPC	15.3 ± 3.4	297	GUVs
Electrodeformation (this study)	DOPC	4.11 ± 2.63	298	GUVs
Probe diffusion (15)	DOPC	0.59 ± 0.2	298	GUVs
Neutron spin echo (9)	DOPC	16.7 ± 1.1	298	SUVs
Electrodeformation (this study)	OMPC	7.73 ± 3.09	298	GUVs
Membrane-anchored particles (16)	13:0 PC	14.7 ± 6.9	297	GUVs
Neutron spin echo (9)	DOPC:Chol (8:2)	31.9 ± 3.5	298	SUVs
Electrodeformation (this study)	DOPC:Chol (1:1)	7.00 ± 4.77	298	GUVs
Electrodeformation (this study)	DPPC:Chol (1:1)	56.4 ± 4.63	298	GUVs
Optical tweezers (80)	DOPC:DPPC (2:1), L_o	2.1	293	bilayer
Shear-driven flow (8)	DOPC:DPPC (85:15), L_d	1.9 ± 11.9	296	GUVs
Shear-driven flow (8)	DiPhyPC:Chol:DPPC (5:40:55), L_o	15.7 ± 9.9	296	GUVs
Domain fluctuations (18)	DiPhyPC:Chol:DPPC (25:55:20)	4 ± 1	293	GUVs
Diffusion of domains (12)	DPPC:DOPC:Chol (3.5:3.5:3), L_o	10–500	295	GUVs
Diffusion of domains (13)	DiPhyPC:DPPC (1:1)	2.2 ± 0.1	296.5	GUVs
Shear-driven flow (19)	DPPC:DOPC:Chol (3:6:1), L_o domain	4.1	293	GUVs
Shear-driven flow (19)	DPPC:DOPC:Chol (4:5:1), L_o domain	14	293	GUVs
Shear-driven flow (19)	DPPC:DOPC:Chol (2:6:2), L_o domain	9.6	293	GUVs
Shear-driven flow (19)	DPPC:DOPC:Chol (4:4:2), L_o domain	4.3	293	GUVs
Shear-driven flow (19)	DPPC:DOPC:Chol (5:3:2), L_o domain	54	293	GUVs
Shear-driven flow (19)	DPPC:DOPC:Chol (6:2:2), L_d domain	1200	293	GUVs
Shear-driven flow (19)	DPPC:DOPC:Chol (2:5:3), L_o domain	7.7	293	GUVs
Shear-driven flow (19)	DPPC:DOPC:Chol (5:2:3), L_d domain	85	293	GUVs
Shear-driven flow (19)	DPPC:DOPC:Chol (6:1:3), L_d domain	1200	293	GUVs
Shear-driven flow (19)	DPPC:DOPC:Chol (3:3:4), L_d domain	0.63	293	GUVs
Shear-driven flow (19)	DPPC:DOPC:Chol (4:2:4), L_d domain	65	293	GUVs
Shear-driven flow (19)	DPPC:DOPC:Chol (5:1:4), L_d domain	71	293	GUVs
Shear-driven flow (19)	DPPC:DOPC:Chol (4:3:3), L_d domain	98	293	GUVs
Shear-driven flow (19)	DPPC:DOPC:Chol (3:5:2), L_o domain	65	293	GUVs
Electrodeformation (this study)	DPPC:DOPC:Chol (1:1:1)	17.7 ± 3.06	298	GUVs
Electrodeformation (this study)	DPPC:DOPC:Chol (1:1:2)	15.4 ± 2.40	298	GUVs
Falling ball viscosimetry (81)	PBd_{33}-*b*-PEO_{20}	1500 ± 120	298	GUVs
Electrodeformation (this study)	PBd_{33}-*b*-PEO_{20}	2890 ± 670	298	GUVs
Micropipette aspiration (82)	PEG-b-PA6ester1	7,900,000 ± 200,000	298	GUVs
Micropipette aspiration (82)	PEG-b-PA444	4,000,000 ± 200,000	298	GUVs
Atomic force microscopy (83)	PBd_{130}-*b*-PEO_{66}	5,000,000	298	bilayer
Atomic force microscopy (83)	PBd_{130}-*b*-PEO_{66} (cross-linked)	20,000,000	298	bilayer
Electrodeformation (this study)	PBd_{13}-*b*-PEO_{11}	14.4 ± 4.40	298	GUVs
Electrodeformation (this study)	PBd_{22}-*b*-PEO_{14}	686 ± 51.0	298	GUVs
Electrodeformation (this study)	PBd_{46}-*b*-PEO_{24}	20,600 ± 4700	298	GUVs
Electrodeformation (this study)	PBd_{54}-*b*-PEO_{29}	46,700 ± 900	298	GUVs
Electrodeformation (this study)	PBd_{120}-*b*-PEO_{78}	157,000 ± 54,500	298	GUVs

L_d and L_o refer to liquid-disordered and liquid-ordered phases, respectively. GUVs, LUVs, and SUVs refer to giant unilamellar vesicles, large unilamellar vesicles, and small unilamellar vesicles, respectively.

[a]For DMPC, SOPC, and DOPC, the bilayer thicknesses are 3.67 nm, 4.00 nm (84), and 3.67 nm (69), respectively. Denotes membrane viscosity obtained from the bulk viscosity, η, using the relation $\eta_m = \eta h$, where h is the bilayer thickness.

AUTHOR CONTRIBUTIONS

H.A.F., R.D., and P.M.V. designed the research; H.A.F. performed the research; H.A.F., R.D., and P.M.V. analyzed the data; H.A.F., R.D., and P.M.V. wrote the paper.

ACKNOWLEDGMENTS

P.M.V. and H.A.F. acknowledge financial support by NIGMS award 1R01GM140461. This research was also supported in part by the National Science Foundation under grant NSF PHY-1748958.

REFERENCES

1. Singer, S. J., and G. L. Nicolson. 1972. The fluid mosaic model of the structure of cell membranes. *Science.* 175:720–731.
2. Cohen, A. E., and Z. Shi. 2020. Do cell membranes flow like honey or jiggle like jello? *BioEssays.* 42:1900142.
3. Le Roux, A.-L., X. Quiroga, …, P. Roca-Cusachs. 2019. The plasma membrane as a mechanochemical transducer. *Philos. Trans. R. Soc. B Biol. Sci.* 374:20180221. https://royalsocietypublishing.org/doi/abs/10.1098/rstb.2018.0221.
4. Illukkumbura, R., T. Bland, and N. W. Goehring. 2020. Patterning and polarization of cells by intracellular flows. *Curr. Opin. Cell*

Biol. 62:123–134. http://www.sciencedirect.com/science/article/pii/S0955067419300924.

5. Sinensky, M. 1974. Homeoviscous adaptation—a homeostatic process that regulates the viscosity of membrane lipids in Escherichia coli. *Proc. Natl. Acad. Sci. U S A.* 71:522–525. https://www.pnas.org/content/71/2/522.
6. Hazel, J. R. 1995. Thermal adaptation in biological membranes: is homeoviscous adaptation the explanation? *Annu. Rev. Physiol.* 57:19–42. https://doi.org/10.1146/annurev.ph.57.030195.000315.
7. Zgorski, A., R. W. Pastor, and E. Lyman. 2019. Surface shear viscosity and interleaflet friction from nonequilibrium simulations of lipid bilayers. *J. Chem. Theory Comput.* 15:6471–6481. https://doi.org/10.1021/acs.jctc.9b00683.
8. Honerkamp-Smith, A. R., F. G. Woodhouse, …, R. E. Goldstein. 2013. Membrane viscosity determined from shear-driven flow in giant vesicles. *Phys. Rev. Lett.* 111:038103. https://link.aps.org/doi/10.1103/PhysRevLett.111.038103.
9. Chakraborty, S., M. Doktorova, …, R. Ashkar. 2020. How cholesterol stiffens unsaturated lipid membranes. *Proc. Natl. Acad. Sci. U S A.* 117:21896–21905.
10. Espinosa, G., I. López-Montero, …, D. Langevin. 2011. Shear rheology of lipid monolayers and insights on membrane fluidity. *Proc. Natl. Acad. Sci. U S A.* 108:6008–6013.
11. Waugh, R. 1982. Surface viscosity measurements from large bilayer vesicle tether formation. II. Experiments. *Biophys. J.* 38:29–37. http://www.sciencedirect.com/science/article/pii/S000634958284527X.
12. Cicuta, P., S. L. Keller, and S. L. Veatch. 2007. Diffusion of liquid domains in lipid bilayer membranes. *J. Phys. Chem. B.* 111:3328–3331.
13. Petrov, E. P., R. Petrosyan, and P. Schwille. 2012. Translational and rotational diffusion of micrometer-sized solid domains in lipid membranes. *Soft Matter.* 8:7552–7555. https://doi.org/10.1039/C2SM25796C.
14. Block, S. 2018. Brownian motion at lipid membranes: a comparison of hydrodynamic models describing and experiments quantifying diffusion within lipid bilayers. *Biomolecules.* 8:30.
15. Herold, C., P. Schwille, and E. P. Petrov. 2010. DNA condensation at freestanding cationic lipid bilayers. *Phys. Rev. Lett.* 104:148102. https://link.aps.org/doi/10.1103/PhysRevLett.104.148102.
16. Hormel, T. T., S. Q. Kurihara, …, R. Parthasarathy. 2014. Measuring lipid membrane viscosity using rotational and translational probe diffusion. *Phys. Rev. Lett.* 112:188101. https://link.aps.org/doi/10.1103/PhysRevLett.112.188101.
17. Jahl, P. E., and R. Parthasarathy. 2021. Assessing the use of ellipsoidal microparticles for determining lipid membrane viscosity. *Biophys. J.* 120:5513–5520. https://doi.org/10.1016/j.bpj.2021.11.020.
18. Camley, B. A., C. Esposito, …, F. L. Brown. 2010. Lipid bilayer domain fluctuations as a probe of membrane viscosity. *Biophys. J.* 99:L44–L46. http://www.sciencedirect.com/science/article/pii/S0006349510008519.
19. Sakuma, Y., T. Kawakatsu, …, M. Imai. 2020. Viscosity landscape of phase-separated lipid membrane estimated from fluid velocity field. *Biophys. J.* 118:1576–1587. http://www.sciencedirect.com/science/article/pii/S0006349520300333.
20. Nagao, M., E. G. Kelley, …, P. D. Butler. 2017. Probing elastic and viscous properties of phospholipid bilayers using neutron spin echo spectroscopy. *J. Phys. Chem. Lett.* 8:4679–4684.
21. Kelley, E. G., P. D. Butler, …, M. Nagao. 2020. Scaling relationships for the elastic moduli and viscosity of mixed lipid membranes. *Proc. Natl. Acad. Sci. U S A.* 117:23365–23373. https://www.pnas.org/content/117/38/23365.
22. Nagao, M., E. G. Kelley, A. Faraone…, 2021. Relationship between viscosity and acyl tail dynamics in lipid bilayers. *Phys. Rev. Lett.* 127:078102. https://doi.org/10.1103/PhysRevLett.127.078102.
23. Wu, Y., M. Štefl, …, M. K. Kuimova. 2013. Molecular rheometry: direct determination of viscosity in Lo and Ld lipid phases via fluorescence lifetime imaging. *Phys. Chem. Chem. Phys.* 15:14986–14993. https://doi.org/10.1039/C3CP51953H.
24. Chwastek, G., E. P. Petrov, and J. P. Sáenz. 2020. A method for high-throughput measurements of viscosity in sub-micrometer-sized membrane systems. *ChemBioChem.* 21:836–844. https://chemistry-europe.onlinelibrary.wiley.com/doi/abs/10.1002/cbic.201900510.
25. Velikov, K., C. Dietrich, …, B. Pouligny. 1997. Motion of a massive microsphere bound to a spherical vesicle. *Europhys. Lett.* 40:405–410. https://doi.org/10.1209/epl/i1997-00479-1.
26. Dimova, R., B. Pouligny, and C. Dietrich. 2000. Pretransitional effects in dimyristoylphosphatidylcholine vesicle membranes: optical dynamometry study. *Biophys. J.* 79:340–356. https://doi.org/10.1016/S0006-3495(00)76296-5.
27. Dimova, R., C. Dietrich, …, B. Pouligny. 1999. Falling ball viscosimetry of giant vesicle membranes: finite-size effects. *Eur. Phys. J. B Condens. Matter Complex Syst.* 12:589–598. https://doi.org/10.1007/s100510051042.
28. den Otter, W., and S. Shkulipa. 2007. Intermonolayer friction and surface shear viscosity of lipid bilayer membranes. *Biophys. J.* 93:423–433. http://www.sciencedirect.com/science/article/pii/S0006349507712961.
29. Vögele, M., J. Köfinger, and G. Hummer. 2018. Hydrodynamics of diffusion in lipid membrane simulations. *Phys. Rev. Lett.* 120:268104. https://link.aps.org/doi/10.1103/PhysRevLett.120.268104.
30. Gurtovenko, A. A., M. Javanainen, …, I. Vattulainen. 2019. The devil is in the details: what do we really track in single-particle tracking experiments of diffusion in biological membranes? *J. Phys. Chem. Lett.* 10:1005–1011. https://doi.org/10.1021/acs.jpclett.9b00065.
31. Danov, K. D., R. Dimova, and B. Pouligny. 2000. Viscous drag of a solid sphere straddling a spherical or flat surface. *Phys. Fluids.* 12:2711–2722. https://aip.scitation.org/doi/abs/10.1063/1.1289692.
32. Naji, A., A. J. Levine, and P. Pincus. 2007. Corrections to the Saffman-Delbrück mobility for membrane bound proteins. *Biophys. J.* 93:L49–L51. https://www.sciencedirect.com/science/article/pii/S0006349507716235.
33. Riske, K. A., and R. Dimova. 2005. Electro-deformation and poration of giant vesicles viewed with high temporal resolution. *Biophys. J.* 88:1143–1155.
34. Aranda, S., K. A. Riske, …, R. Dimova. 2008. Morphological transitions of vesicles induced by AC electric fields. *Biophys. J.* 95:L19–L21.
35. Salipante, P. F., and P. M. Vlahovska. 2014. Vesicle deformation in DC electric pulses. *Soft Matter.* 10:3386–3393.
36. Yu, M., R. B. Lira, …, H. Lin. 2015. Ellipsoidal relaxation of deformed vesicles. *Phys. Rev. Lett.* 115:128303.
37. Deschamps, J., V. Kantsler, …, V. Steinberg. 2009. Dynamics of a vesicle in general flow. *Proc. Natl. Acad. Sci. U S A.* 106:11444–11447.
38. Shenoy, A., C. V. Rao, and C. M. Schroeder. 2016. Stokes trap for multiplexed particle manipulation and assembly using fluidics. *Proc. Natl. Acad. Sci. U S A.* 113:3976–3981.
39. Kumar, D., C. M. Richter, and C. M. Schroeder. 2020. Conformational dynamics and phase behavior of lipid vesicles in a precisely controlled extensional flow. *Soft Matter.* 16:337–347. https://doi.org/10.1039/C9SM02048A.
40. Guck, J., R. Ananthakrishnan, …, J. Käs. 2001. The optical stretcher: a novel laser tool to micromanipulate cells. *Biophys. J.* 81:767–784. https://www.sciencedirect.com/science/article/pii/S0006349501757402.
41. Delabre, U., K. Feld, …, J. Guck. 2015. Deformation of phospholipid vesicles in an optical stretcher. *Soft Matter.* 11:6075–6088. https://doi.org/10.1039/C5SM00562K.
42. Kummrow, M., and W. Helfrich. 1991. Deformation of giant lipid vesicles by electric fields. *Phys. Rev. A.* 44:8356–8360. https://link.aps.org/doi/10.1103/PhysRevA.44.8356.
43. Niggemann, G., M. Kummrow, and W. Helfrich. 1995. The bending rigidity of phosphatidylcholine bilayers: dependences on experimental method, sample cell sealing and temperature. *J. Phys. France.* 5:413–425. https://doi.org/10.1051/jp2:1995141.
44. Gracia, R. S., N. Bezlyepkina, …, R. Dimova. 2010. Effect of cholesterol on the rigidity of saturated and unsaturated membranes:

fluctuation and electrodeformation analysis of giant vesicles. *Soft Matter.* 6:1472–1482. https://doi.org/10.1039/B920629A.

45. Faizi, H. A., R. Dimova, and P. M. Vlahovska. 2021. Electromechanical characterization of biomimetic membranes using electrodeformation of vesicles. *Electrophoresis.* 42:2027–2032.
46. Henle, M. L., and A. J. Levine. 2009. Effective viscosity of a dilute suspension of membrane-bound inclusions. *Phys. Fluids.* 21:033106. https://doi.org/10.1063/1.3086831.
47. Woodhouse, F. G., and R. E. Goldstein. 2012. Shear-driven circulation patterns in lipid membrane vesicles. *J. Fluid Mech.* 705:165–175.
48. Rahimi, M., A. DeSimone, and M. Arroyo. 2013. Curved fluid membranes behave laterally as effective viscoelastic media. *Soft Matter.* 9:11033–11045. https://doi.org/10.1039/C3SM51748A.
49. Sigurdsson, J. K., and P. J. Atzberger. 2016. Hydrodynamic coupling of particle inclusions embedded in curved lipid bilayer membranes. *Soft Matter.* 12:6685–6707. https://doi.org/10.1039/C6SM00194G.
50. Vlahovska, P. M., and C. Misbah. 2019. Theory of vesicle dynamics in flow and electric fields. *In* The Giant Vesicle Book. R. Dimova and C. Marques, eds. CRC Press, Chapter 7.
51. Vlahovska, P. M. 2010. Non-equilibrium dynamics of lipid membranes: deformation and stability in electric fields. *In* Advances in Planar Lipid Bilayers and Liposomes. A. Iglic, ed. Elsevier, pp. 103–146.
52. Vlahovska, P. M. 2016. Dynamics of membrane bound particles: capsules and vesicles. *In* Low-Reynolds-Number Flows: Fluid-Structure Interactions. C. Duprat and H. Stone, eds. Royal Society of Chemistry.
53. Angelova, M. I., and D. S. Dimitrov. 1986. Liposome electroformation. *Faraday Discuss. Chem. Soc.* 81:303–311. https://doi.org/10.1039/DC9868100303.
54. Faizi, H. A., S. L. Frey, …, P. M. Vlahovska. 2019. Bending rigidity of charged lipid bilayer membranes. *Soft Matter.* 15:6006–6013. https://doi.org/10.1039/C9SM00772E.
55. Faizi, H. A., C. J. Reeves, …, R. Dimova. 2020. Fluctuation spectroscopy of giant unilamellar vesicles using confocal and phase contrast microscopy. *Soft Matter.* 16:8996–9001. https://doi.org/10.1039/D0SM00943A.
56. Lacoste, D., G. I. Menon, …, J. F. Joanny. 2009. Electrostatic and electrokinetic contributions to the elastic moduli of a driven membrane. *Eur. Phys. J. E.* 28:243–264.
57. Salipante, P. F., M. L. Shapiro, and P. M. Vlahovska. 2015. Electric field induced deformations of biomimetic fluid membranes. *Procedia IUTAM.* 16:60–69.
58. Veatch, S. L., and S. L. Keller. 2002. Organization in lipid membranes containing cholesterol. *Phys. Rev. Lett.* 89:268101.
59. Veatch, S. L., and S. L. Keller. 2005. Seeing spots: complex phase behavior in simple membranes. *Biochim. Biophys. Acta.* 1746:172–185.
60. Uppamoochikkal, P., S. Tristram-Nagle, and J. F. Nagle. 2010. Orientation of tie-lines in the phase diagram of DOPC/DPPC/cholesterol model biomembranes. *Langmuir.* 26:17363–17368. https://doi.org/10.1021/la103024f.
61. Gambin, Y., R. Lopez-Esparza, …, W. Urbach. 2006. Lateral mobility of proteins in liquid membranes revisited. *Proc. Natl. Acad. Sci. U S A.* 103:2098–2102. https://www.pnas.org/content/103/7/2098.
62. Scherfeld, D., N. Kahya, and P. Schwille. 2003. Lipid dynamics and domain formation in model membranes composed of ternary mixtures of unsaturated and saturated phosphatidylcholines and cholesterol. *Biophys. J.* 85:3758–3768. http://www.sciencedirect.com/science/article/pii/S0006349503747912.
63. Saffman, P. G., and M. Delbrück. 1975. Brownian motion in biological membranes. *Proc. Natl. Acad. Sci. U S A.* 72:3111–3113. https://www.pnas.org/content/72/8/3111.
64. Tristram-Nagle, S., H. I. Petrache, and J. F. Nagle. 1998. Structure and interactions of fully hydrated dioleoylphosphatidylcholine bilayers. *Biophys. J.* 75:917–925. http://www.sciencedirect.com/science/article/pii/S0006349598775800.
65. Nagle, J. F., and S. Tristram-Nagle. 2000. Structure of lipid bilayers. *Biochim. Biophys. Acta Rev. Biomembr.* 1469:159–195. http://www.sciencedirect.com/science/article/pii/S0304415700000162.
66. Liu, Y., and J. F. Nagle. 2004. Diffuse scattering provides material parameters and electron density profiles of biomembranes. *Phys. Rev. E.* 69:040901. https://link.aps.org/doi/10.1103/PhysRevE.69.040901.
67. Kucerka, N., S. Tristram-Nagle, and J. F. Nagle. 2006. Structure of fully hydrated fluid phase lipid bilayers with monounsaturated chains. *J. Membr. Biol.* 208:193–202. https://doi.org/10.1007/s00232-005-7006-8.
68. Kučerka, N., J. F. Nagle, …, J. Katsaras. 2008. Lipid bilayer structure determined by the simultaneous analysis of neutron and X-ray scattering data. *Biophys. J.* 95:2356–2367. http://www.sciencedirect.com/science/article/pii/S0006349508783838.
69. Pan, J., T. T. Mills, …, J. F. Nagle. 2008. Cholesterol perturbs lipid bilayers nonuniversally. *Phys. Rev. Lett.* 100:198103. https://link.aps.org/doi/10.1103/PhysRevLett.100.198103.
70. Camley, B. A., and F. L. H. Brown. 2019. Motion of objects embedded in lipid bilayer membranes: advection and effective viscosity. *J. Chem. Phys.* 151:124104.
71. Discher, D. E., and F. Ahmed. 2006. Polymersomes. *Annu. Rev. Biomed. Eng.* 8:323–341.
72. LoPresti, C., H. Lomas, …, G. Battaglia. 2009. Polymersomes: nature inspired nanometer sized compartments. *J. Mater. Chem.* 19:3576–3590. https://doi.org/10.1039/B818869F.
73. Boal, D. 2002. Mechanics of the Cell. Cambridge University Press.
74. Rawicz, W., K. Olbrich, …, E. Evans. 2000. Effect of chain length and unsaturation on elasticity of lipid bilayers. *Biophys. J.* 79:328–339.
75. Bermudez, H., A. K. Brannan, …, D. E. Discher. 2002. Molecular weight dependence of polymersome membrane structure, elasticity, and stability. *Macromolecules.* 35:8203–8208. https://doi.org/10.1021/ma020669l.
76. Fischer, P., and P. Erni. 2007. Emulsion drops in external flow fields - the role of liquid interfaces. *Curr. Opin. Colloid Interface Sci.* 12:196–205.
77. Guzman, E., J. Tajuelo, …, R. G. Rubio. 2018. Shear rheology of fluid interfaces: closing the gap between macro- and micro-rheology. *Curr. Opin. Colloid Interface Sci.* 37:33–48.
78. Jaensson, N., and J. Vermant. 2018. Tensiometry and rheology of complex interfaces. *Curr. Opin. Colloid Interface Sci.* 37:136–150. https://www.sciencedirect.com/science/article/pii/S1359029418300062.
79. Nojima, Y., and K. Iwata. 2014. Viscosity heterogeneity inside lipid bilayers of single-component phosphatidylcholine liposomes observed with picosecond time-resolved fluorescence spectroscopy. *J. Phys. Chem. B.* 118:8631–8641. https://doi.org/10.1021/jp503921e.
80. Amador, G. J., D. van Dijk, …, D. Tam. 2021. Hydrodynamic shear dissipation and transmission in lipid bilayers. *Proc. Natl. Acad. Sci. U S A.* 118. https://www.pnas.org/content/118/21/e2100156118.
81. Dimova, R., U. Seifert, …, H.-G. Döbereiner. 2002. Hyperviscous diblock copolymer vesicles. *Eur. Phys. J. E.* 7:241–250. https://doi.org/10.1140/epje/i200101032.
82. Mabrouk, E., D. Cuvelier, …, M.-H. Li. 2009. Formation and material properties of giant liquid crystal polymersomes. *Soft Matter.* 5:1870–1878. https://doi.org/10.1039/B815817G.
83. Kocun, M., W. Mueller, …, A. Janshoff. 2010. Viscoelasticity of pore-spanning polymer membranes derived from giant polymersomes. *Soft Matter.* 6:2508–2516. https://doi.org/10.1039/B924650A.
84. Kučerka, N., M.-P. Nieh, and J. Katsaras. 2011. Fluid phase lipid areas and bilayer thicknesses of commonly used phosphatidylcholines as a function of temperature. *Biochim. Biophys. Acta Biomembr.* 1808:2761–2771. https://www.sciencedirect.com/science/article/pii/S0005273611002276.

Biophysical Journal, Volume *121*

Supplemental information

A vesicle microrheometer for high-throughput viscosity measurements of lipid and polymer membranes

Hammad A. Faizi, Rumiana Dimova, and Petia M. Vlahovska

Supplementary Material: A vesicle microrheometer for high-throughput viscosity measurements of lipid and polymer membranes

Hammad A. Faizi,[1] Rumiana Dimova,[2] and Petia M. Vlahovska[3]

[1] *Department of Mechanical Engineering, Northwestern University, Evanston, IL 60208, USA*
[2] *Department of Theory and Biosystems, Max Planck Institute of Colloids and Interfaces, Science Park Golm, 14424 Potsdam, Germany*
[3] *Department of Engineering Sciences and Applied Mathematics, Northwestern University, Evanston, IL, 60208, USA, email: petia.vlahovska@northwestern.edu*

1. SHAPE EVOLUTION OF QUASI-SPHERICAL VESICLE IN A UNIFORM ELECTRIC FIELD

A. Summary of the theoretical model

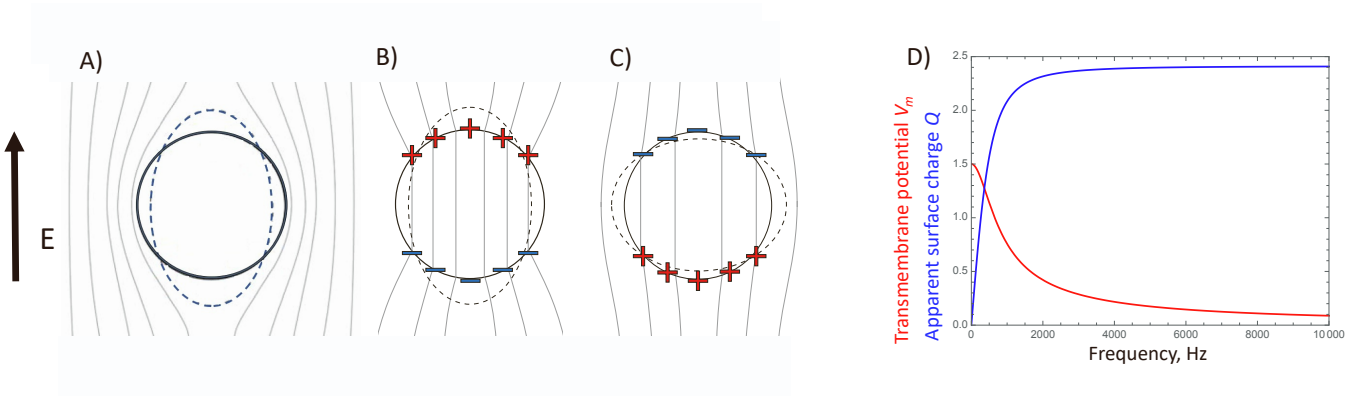

Fig. S 1: (A)-(C) Physical mechanisms of the frequency-dependent membrane polarization and vesicle dipole in an applied uniform AC field. The lines correspond to constant electric field. Upon application of an external electric field, charges accumulate on the two sides of the membrane setting up a potential difference, i.e., the membrane acts as a capacitor. (A) At low frequencies, $\omega \ll \omega_c$, the membrane capacitor is fully charged, the induced charge density on the two membrane surfaces is the same but of opposite sign. (B) and (C) At intermediate frequencies, $\omega > \omega_c$, it is short-circuited and there is charge imbalance between the inner and outer membrane surfaces $Q = \varepsilon E_0 Q_0 \cos\theta$. (B) If the enclosed solution is more conducting than the suspending medium, $\Lambda > 1$, vesicle is pulled into an prolate ellipsoid. (C) The polarization is reversed in the opposite case $\Lambda < 1$ and the vesicle deforms into an oblate ellipsoid. (D) Variation with frequency of the transmembrane potential (red) and apparent charge at the pole (blue).

Let us consider a vesicle made of a charge-free lipid bilayer membrane with bending rigidity κ, tension $\sigma_{\rm eq}$, capacitance $C_{\rm m}$. The vesicle is suspended in a solution with conductivity $\lambda_{\rm ex}$ and permittivity $\varepsilon_{\rm ex}$, and filled with a different solution characterized by $\lambda_{\rm in}$ and $\varepsilon_{\rm in}$.

An axisymmetric stress, such as generated by uniform electric field or extensional flow, deforms the vesicle into a spheroid with symmetry axis aligned with the extensional axis. The spheroid aspect ratio is $\nu = a/b$, where a is the length of the symmetry axis and b is the length of the axis perpendicular to the symmetry axis. For small deformations, $\nu \lesssim 1.3$, the shape is well approximated by

$$r_s(\theta) = R\left(1 + \frac{s}{2}\left(1 + 3\cos 2\theta\right)\right), \tag{S1}$$

where r_s is the position of the surface, R is the initial radius of the vesicle, s is the deformation parameter, and θ is the angle with the applied field direction; $\theta = 0$ and $\pi/2$ correspond to the pole and the equator, respectively. The ellipsoid aspect ratio is related to the deformation parameter by $\nu = (1+s)/(1-2s)$.

The theory developed by *Vlahovska et al.* [1–4] predicts that the deformation parameter evolution is given by the balance of imposed and membrane stresses

$$\dot{s} = \frac{1}{32 + 23\chi + 16\chi_m}\left(\frac{\varepsilon_{\rm ex} E_0^2 p^{\rm el}}{\eta} - 24 s(6\kappa + \sigma(s)R^2)\frac{1}{\eta R^3}\right) \tag{S2}$$

For small deformations, $s \ll 1$, $\nu \sim 1 + 3s$ and the above equation yields Eq. 1 in the main text.

The AC field, $E(t) = E_0 \sin(\omega t)$, generates an electric stress which has two components, a steady one $p^{\rm el}$ and an oscillatory one with frequency twice the applied one

$$p = p^{\rm el} + p^c_\omega \cos(2\omega t) + p^s_\omega \sin(2\omega t)$$

In the experiments typically $\bar{\omega} \gg 1$ and the oscillatory component only drives very small oscillations about the deformation induced by the steady stress component.

The steady electric stress is given by

$$p^{\rm el} = 2(1 - P^r_{\rm ex}) + \frac{1}{2} P^2_{\rm ex} - 2SP^2_{\rm in} \tag{S3}$$

and the amplitudes of the unsteady stress are

$$\begin{aligned} p^c_\omega &= \frac{1}{2}\left(4(1 - P^r_{\rm ex}) - \left(P^i_{\rm ex}\right)^2 + \left(P^r_{\rm ex}\right)^2 - 4S\left(\left(P^i_{\rm in}\right)^2 + \left(P^r_{\rm in}\right)^2\right)\right) \\ p^s_\omega &= 2P^i_{\rm ex} - P^i_{\rm ex}P^r_{\rm ex} + 4SP^i_{\rm in}P^r_{\rm in} \end{aligned} \tag{S4}$$

where

$$\begin{aligned} P_{\rm ex} =& \frac{K_{\rm ex} + K_{\rm in}(V_m - 1)}{K_{\rm in} + 2K_{\rm ex}}, \quad P_{\rm in} = \frac{K_{\rm ex}(3 - 2V_m)}{K_{\rm in} + 2K_{\rm ex}}, \\ V_m =& \frac{3K_{\rm in}K_{\rm ex}}{2K_{\rm in}K_{\rm ex} + {\rm i}C_{\rm m}\left(K_{\rm in} + 2K_{\rm ex}\right)\bar{\omega}} \end{aligned} \tag{S5}$$

Here $\bar{\omega} = \omega\varepsilon_{\rm ex}/\lambda_{\rm ex}$ and $\bar{C}_{\rm m} = C_{\rm m}R/\varepsilon_{\rm ex}$ are the dimensionless frequency and membrane capacitance. $K_{\rm in} = 1 + {\rm i}\bar{\omega}$ and $K_{\rm ex} = \Lambda + {\rm i}\bar{\omega}S$ are the dimensionless complex permittivities. $S = \varepsilon_{\rm in}/\varepsilon_{\rm ex}$ and $\Lambda = \lambda_{\rm in}/\lambda_{\rm ex}$ are the ratios of permittivities and conductivities of the fluids interior and exterior to the vesicle. P^r and P^i denote the real and imaginary part of P, and $P^2 = PP^*$, where the superscript * denotes complex conjugate. The electric stress in DC field is obtained by setting $\bar{\omega} = 0$ and the electric field amplitude to $E_0\sqrt{2}$.

Typically, both the inner and outer fluids are aqueous solutions with similar permittivities, $\varepsilon_{\rm in} \approx \varepsilon_{\rm ex} = \varepsilon$, hence S can be set to 1. In this case Eq. S3 reduces to

$$p^{\rm el} = \frac{9\left[\bar{\omega}^2\left(\bar{C}^2_{\rm m}(\Lambda+2)^2(\Lambda-1)(\Lambda+3) + 2\bar{C}_{\rm m}\Lambda\left(\Lambda^2+\Lambda-2\right) + 9\Lambda^2\right) + \Lambda^2(\Lambda+2)^2\right]}{2\left((\Lambda+2)^2 + 9\bar{\omega}^2\right)\left(\bar{C}^2_{\rm m}(\Lambda+2)^2\bar{\omega}^2 + 4\Lambda^2\right)}, \tag{S6}$$

where $\bar{\sigma} = \sigma R^2/\kappa$. At low frequencies, $\bar{\omega} \to 0$, the membrane capacitor is fully charged, and $p^{\rm el} = 9/16$ and we obtain Equation 1 in the main text.

The imbalance between the induced charge of the two membrane surfaces is $Q = \varepsilon E_0 Q_0 \cos\theta$, where the maximum charge is

$$Q_0 = \frac{3\bar{\omega}C_m(\Lambda-1)(\Lambda+2)}{\left[\left((2+\Lambda)^2 + 9\bar{\omega}^2\right)\left(4\Lambda^2 + C^2_m\bar{\omega}^2(2+\Lambda)^2\right)\right]^{1/2}} \tag{S7}$$

At low frequencies, $\bar{\omega} \to 0$ the charge imbalance vanishes.

B. Linear approximation of the evolution equation

The tension in Eq. S2 is of entropic origin and depends nonlinearly on deformation [5]. For a quasi-spherical vesicle

$$\sigma = \sigma_0 \exp\left(\frac{8\pi\kappa}{k_B T}\alpha\right) \tag{S8}$$

where $\alpha = (A - A_0)/A_0$ is the area strain (the difference between the area of the deformed vesicle A and a sphere with the same volume A_0). For small deformations, $\alpha = 8s^2/5$ [6]. For aspect ratios smaller than 1.1, such as during the early deformation, the area strain is very small and tension remains close to the equilibrium tension σ_0. Assuming constant tension, Eq. 2 in the main text can be integrated to yield

$$\nu(t) = 1 + \frac{pR}{24\sigma}\left(1 - \exp\left(-\frac{24\sigma}{\eta R\left(55 + 16\chi_m\right)}t\right)\right) \tag{S9}$$

If

$$\frac{24\sigma t}{\eta R\,(55+16\chi_m)} \ll 1$$

the exponent is expanded in Taylor series to yield the linear evolution, Eq. 2 in the main text.

The time limit for the linear approximation can be estimated by comparing the linear and quadratic terms in the Taylor series of the exponential term in Eq. S9. The Taylor series of the exponential function is

$$\exp(-ct) = 1 - ct + \frac{(ct)^2}{2} + h.o.t. \quad \text{where for Eq. S9} \quad c = \frac{24\sigma}{\eta R\,(55+16\chi_m)}$$

It shows that the quadratic correction becomes comparable to the linear term when

$$ct = \frac{(ct)^2}{2} \Longrightarrow t = \frac{2}{c}$$

which gives the estimate for the time up to which the linear approximation is reasonable

$$\frac{t}{t_\mathrm{d}} = \frac{\varepsilon E_0^2 R\,(55+16\chi_m)}{12\sigma}$$

Considering typical parameters, $\sigma_0 = 10^{-8}$ N/m, $\kappa = 25k_BT$, $E_0 = 10$ kV/m, $R = 10\,\mu$m gives $\varepsilon E_0^2 R/\sigma \sim 1$, where σ is evaluated from Eq. S8 using aspect ratio $\nu = 1.2$. Thus the linear regime extends to $t/t_\mathrm{d} \sim 1$ if $\chi_m \sim 1$. Higher membrane viscosity lengthens the linear deformation regime, e.g., if $\chi_m \sim 10$, as in polymersomes made of PBd_{22}-*b*-PEO_{14}, the cut-off time becomes $t/t_\mathrm{d} \sim 15$, see Fig. Fig. S2a

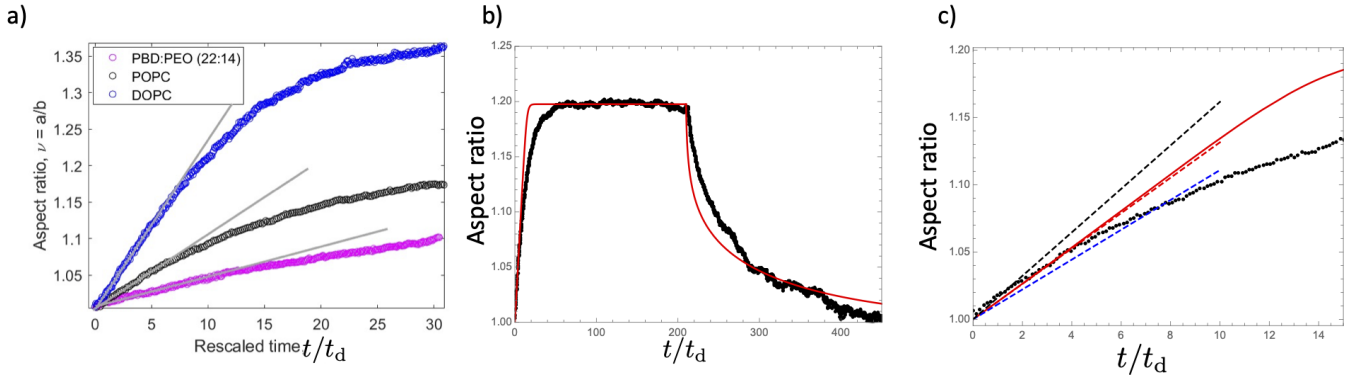

Fig. S 2: a) Vesicle deformation as a function of the dimensionless time t/t_d. (b) Fit of the deformation/relaxation curve of the POPC vesicle shown on Figure 1 in the main text. Solid line is computed from Eq. S2 with parameters $\chi_m = 10$ while field is on, $\chi_m = 0$ after the field is turned off, bending rigidity $\kappa = 25k_BT$ and initial tension $\sigma_0 = 3 \times 10^{-8}$ N/m. (c) Zoom into the initial deformation showing the initial slopes $\chi_m = 10$ (red) and $\pm 25\%$ deviation, $\chi_m = 12.5$ (black) and $\chi_m = 7.5$ (blue).

In principle, Eq. S2 could be used to fit he whole deformation and relaxation curve (note that Eq. S9 is an approximation derived from Eq. S2 assuming constant tension, which implies very small vesicle deformation, aspect ratio <1.1) If the whole data set were to be used, this would require a nonlinear fit using Eq. S2 (since it can not be analytically integrated to give $\nu(t)$ because tension increases exponentially with area strain, see Eq. S8) with at least two parameters – viscosity and initial tension (if bending rigidity is known). Such fit is challenging. Furthermore, the effect of the deformation in the theory (second term in Eq. S2) is an approximation - it only includes the linear correction for the deviation from a sphere and as a result there is an error introduced by neglecting the higher order terms; this error can become significant as aspect ratio increases. Figure Fig. S2b,c does show that the theory does not match well the vesicle deformation at times where the tension is operational, indicating limitations of the theory that likely arise from a break-down of the small deformation assumption and/or modification of the membrane elastic properties (tension and bending rigidity) by the electric field (for example, there could be an electric field induced contribution to the tension [7, 8])

Thus, the errors arising from the nonlinear fit and the shape approximation are likely to negatively affect the accuracy with which the viscosity is determined. It is really fortuitous that vesicles have the initial linear deformation regime, due to their very low tension, which leads to a large difference between the rate with which electric stresses deform the vesicle,$t_\mathrm{d}^{-1} \sim \eta/\varepsilon E_0^2$, and the rate with which the tension pulls the vesicle back to its equilibrium spherical shape,$t_\sigma^{-1} \sim \eta R/\sigma_0$. The ratio of these two rates $t_\mathrm{d}^{-1}/t_\sigma^{-1} = \sigma/\varepsilon E_0^2 R \gg 1$ indicates that the initial deformation is entirely dominated by the electric stresses (and insensitive to tension).

2. ADDITIONAL DATA

A. Batch reproducibility for homogeneous (DOPC) and mixed membrane compositions (DOPC:DPPC:Chol (1:1:1))

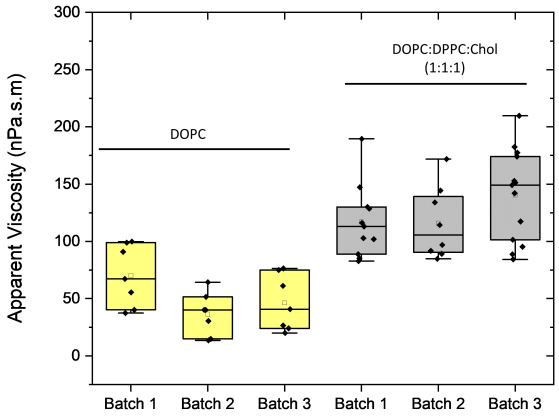

Fig. S 3: Method reproducibility for the same system across different batches: Membrane viscosity for DOPC and DOPC:DPPC:Chol (1:1:1) for three different batches of prepared vesicles. The applied frequency and field strength are 1 kHz and 10 kV/m for respectively. For DOPC:DPPC:Chol (1:1:1), the applied frequency is 2 kHz and and applied field strength is 6 kV/m. The solid symbols show measurements on individual vesicles. The box-plot represents the standardized distribution of data based on five numbers minimum value, first quartile (Q1), median, third quartile (Q3), and maximum value. The open square represents the mean value. The numerical data is summarized in Table S3.

Figure Fig. S3 shows the box plot presentation for apparent membrane viscosity values obtained for the same system across three different batches of vesicles prepared from DOPC and DOPC:DPPC:Chol (1:1:1). The zero charge or frequency membrane viscosity data is given in the main text.

B. Deformation curves of bilayers at different field strength and frequency

Figure Fig. S4A represents deformation curves of POPC vesicles at different field strength (6-10 kV/m) at frequency 1 kHz. In Figure Fig. S4B the data is re-plotted again in rescaled time with t_{d}. The inverse of t_{d} can be expressed as shear rate, $\dot{\gamma}$ which in this case ranges from, $\dot{\gamma}$ ∼10-100 s^{-1}. The collapse of the data on single curve indicates that the deformation rate of POPC bilayers are not affected at a given shear rate and they exhibit Newtonian rheology.

Eq. 2 in the main text shows that the slope depends on t_{d}, which depends on the field amplitude E_0, and p^{el}, which depends on frequency. Hence to isolate the viscosity, one needs to plot the deformation data as a function of time rescaled as $t/t_{\mathrm{d}}p^{\mathrm{el}}$, see Figure Fig. S5.

C. Bending rigidity values from Flickering Spectroscopy and capacitance measurements for electrodeformation method

The method for flickering spectroscopy is detailed in [9, 10]. Here, we summarize the electrodeformation method to extract out membrane capacitance. The procedure follows the original approach developed by *Salipante et al.* [11]. The vesicle shape morphology with conductivity ratio $\Lambda > 1$ is always prolate. However, for $\Lambda < 1$, the conductivity of the outer solution is higher than the vesicle solution and the aspect ratio/deformation parameter $s(\omega)$ is positive at low frequencies that is prolate shape. As the frequency increases, the vesicles becomes less prolate and adopts a spherical shape at a certain frequency. Above this critical frequency, the vesicles adopt an oblate shape. The critical frequency can be approximated as:

$$\omega_c = \frac{\lambda_{\mathrm{in}}}{RC_{\mathrm{m}}} \frac{1}{\sqrt{(1-\Lambda)(3+\Lambda)}} \tag{10}$$

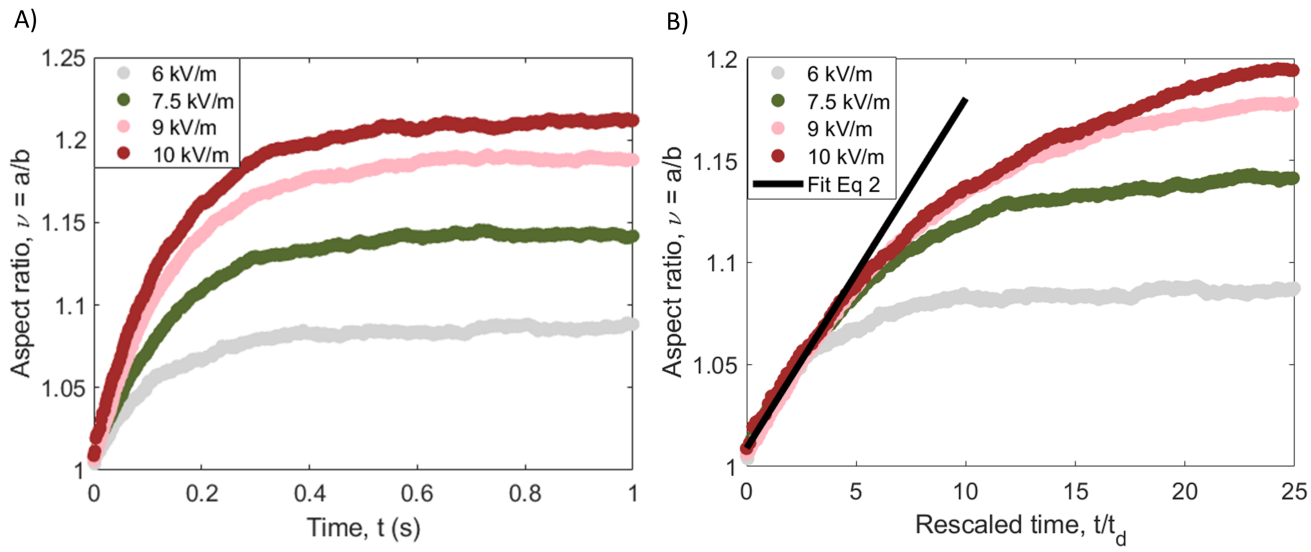

Fig. S 4: (A) Deformation curves for a POPC vesicle (R= 30.1 μm) exposed to fields of different amplitudes (at 1 kHz). (B) The initial slope of the data in (A) re-plotted as a function of the re-scaled time $t/t_{\rm d}$ yields an apparent membrane viscosity $\eta_m = 2.63 \pm 0.41 \times 10^{-7}$ Pa.s.m.

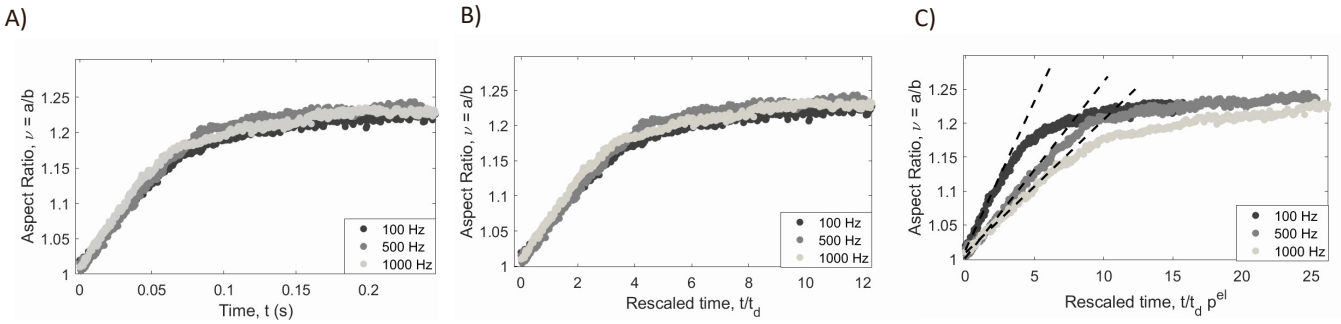

Fig. S 5: (A) Deformation curves for a POPC vesicle (R= 14.7 μm) exposed to fields of different frequency but same field amplitude $E_0 = 8$ kV/m. (B) The initial slope of the data in (A) re-plotted as a function of the re-scaled time $t/t_{\rm d}$, see Figure Fig. S5. The electric stress $p^{\rm el}$ increases with frequency but the slope in (B) remains the same indicating that apparent surface viscosity also increases. (C) Indeed, when data are plotted vs $t/t_{\rm d}p^{\rm el}$ the slope decreases with increasing frequency yielding the frequency dependence of the apparent viscosity. Extrapolation to zero frequency gives the membrane viscosity

Hence, the membrane capacitance can be determined from the experimentally measured critical frequency based on prolate-oblate transition with a frequency sweep [11]. The measured bending rigidity and capacitance values are summarized in Table I.

Table S I: Membrane bending rigidity and capacitance of phospholipids, polymers PBd_x-*b*-PEO_y and mixed system of DOPC:DPPC:Chol at 25 ^{o}C determined in this study. Bending rigidity was measured with flickering spectroscopy and membrane capacitance was measured with the electrodeformation method. M_w and M_h refer to the total and hydrophobic molecular weight, respectively. NA means not available.

Composition	M_w [kDa]	M_h [kDa]	κ ($k_B\,T$)	C_m ($\mu F/cm^2$)
POPC	0.760	0.448	27.8 ±2.3	0.72 ± 0.04
SOPC	0.787	0.476	30.1 ±3.1	0.71 ± 0.02
DOPC	0.786	0.474	22.2 ±2.0	0.72 ± 0.04
OMPC	0.732	0.420	27.1 ±2.6	0.71 ± 0.03
DOPC:Chol (1:1)	NA	NA	27.8 ±4.6	0.50 ± 0.09
DPPC:Chol (1:1)	NA	NA	121.3 ±11.0	0.45 ± 0.05
DOPC:DPPC:Chol (1:1:1)	NA	NA	72.0 ±8.4	0.51 ± 0.16
DOPC:DPPC:Chol (1:1:2)	NA	NA	69.2 ±7.9	0.63 ± 0.10
PBd_{13}-*b*-PEO_{11}	1.19	0.7	17.1 ±1.5	0.36 ± 0.05
PBd_{22}-*b*-PEO_{14}	1.80	1.35	31.0 ±5.1	0.27 ± 0.03
PBd_{33}-*b*-PEO_{20}	2.60	1.85	54.4 ±6.4	0.23 ± 0.04
PBd_{46}-*b*-PEO_{24}	3.54	2.60	NA	0.18 ± 0.03
PBd_{54}-*b*-PEO_{29}	4.19	3.10	154± 16.0	0.18 ± 0.04
PBd_{120}-*b*-PEO_{78}	9.91	6.80	NA	0.07 ± 0.01

Table S II: Membrane viscosities and values of a dye diffusion coefficient (DiC18) for the DOPC:DPPC:Chol ternary system. The values in brackets indicate lipid molar ratios (first column) and the number of measured vesicles (third column). All the experiments were performed at 25.0 ^{o}C. L_d and L_o denote liquid disordered and liquid ordered, respectively. The diffusion coefficient were taken from [12]

Multi-component	Phase state	η_m [nPa.s.m]	D [μm^2/s [12]]
DOPC	L_d	4.11 ±2.63 (20)	6.30±0.13
DPPC:Chol (1:1)	L_o	56.4 ±4.63 (25)	0.48±0.06
DOPC:DPPC:Chol (1:1:2)	L_o	15.4 ±2.40 (25)	1.85±0.13
DOPC:DPPC:Chol (1:1:1)	L_d	17.7 ±3.06 (18)	2.50±0.20
DOPC:Chol (1:1)	L_d	7.00 ±4.77 (25)	3.25±0.25

3. MOVIE DESCRIPTION

Videos showing the deformation and relaxation of GUVs made of POPC (left) and PBd_{33}-*b*-PEO_{20} (right) with radii of 31 and 24 μm, respectively. The videos were acquired with phase contrast microscopy at E_o= 10 kV/m at 1 kHz. The time stamps show the actual time.

[1] P. M. Vlahovska, R. S. Gracia, S. Aranda-Espinoza, and R. Dimova. Electrohydrodynamic model of vesicle deformation in alternating electric fields. Biophys. J., 96:4789–4803, 2009.

[2] P. M. Vlahovska. Non-equilibrium dynamics of lipid membranes: deformation and stability in electric fields. In A. Iglic, editor, Advances in Planar Lipid Bilayers and Liposomes, vol. 12, pages 103–146. Elsevier, 2010.

[3] Petia M. Vlahovska. Electrohydrodynamics of drops and vesicles. Annu. Rev. Fluid Mech., 51:305–330, 2019.

[4] Petia M. Vlahovska and C. Misbah. Theory of vesicle dynamics in flow and electric fields. In R. Dimova and C. Marques, editors, The Giant Vesicle Book, page Chapter 7. CRC Press, 2019.

[5] E. Evans and W. Rawicz. Entropy driven tension and bending elasticity in condensed-fluid membranes. Phys. Rev. Lett., 64:2094–2097, 1990.

[6] U. Seifert. Fluid membranes in hydrodynamic flow fields: Formalism and an application to fluctuating quasispherical vesicles. Eur. Phys. J. B, 8:405–415, 1999.

[7] D. Needham and R. M. Hochmuth. Electromechanical permeabilization of lipid vesicles. role of membrane tension and compressibility. Biophys. J., 55:1001–1009, 1989.

[8] Rumiana Dimova, Natalya Bezlyepkina, Marie Domange Jordö, Roland L. Knorr, Karin A. Riske, Margarita Staykova, Petia M. Vlahovska, Tetsuya Yamamoto, Peng Yang, and Reinhard Lipowsky. Vesicles in electric fields: Some novel aspects of membrane behavior. Soft Matter, 5:3201–3212, 2009. doi:10.1039/B901963D. URL `http://dx.doi.org/10.1039/B901963D`.

[9] Hammad A. Faizi, Shelli L. Frey, Jan Steinkühler, Rumiana Dimova, and Petia M. Vlahovska. Bending rigidity of charged lipid bilayer membranes. Soft Matter, 15(29):6006–6013, 2019. ISSN 1744-683X. doi:10.1039/C9SM00772E. URL `http://dx.doi.org/10.1039/C9SM00772E`.

[10] Hammad A. Faizi, Cody J. Reeves, Vasil N. Georgiev, Petia M. Vlahovska, and Rumiana Dimova. Fluctuation spectroscopy of giant unilamellar vesicles using confocal and phase contrast microscopy. Soft Matter, 16:8996–9001, 2020. doi:10.1039/D0SM00943A. URL `http://dx.doi.org/10.1039/D0SM00943A`.

[11] P. F. Salipante, R. Knorr, R. Dimova, and P. M. Vlahovska. Electrodeformation method for measuring the capacitance of bilayer membranes. Soft Matter, 8:3810– 3816, 2012.

[12] Dag Scherfeld, Nicoletta Kahya, and Petra Schwille. Lipid dynamics and domain formation in model membranes composed of ternary mixtures of unsaturated and saturated phosphatidylcholines and cholesterol. Biophysical Journal, 85(6):3758 – 3768, 2003. ISSN 0006-3495. doi:https://doi.org/10.1016/S0006-3495(03)74791-2. URL `http://www.sciencedirect.com/science/article/pii/S0006349503747912`.